CHEMICAL ENGINEERING TRANSACTIONS
VOL. 111, 2024
A publication of AIDIC
The Italian Association of Chemical Engineering
Online at www.cetjournal.it
Guest Editors: Valerio Cozzani, Bruno Fabiano, Genserik Reniers

ISBN 979-12-81206-11-3; **ISSN** 2283-9216
DOI: 10.3303/CET24111085

Assessment of RANS Turbulence Models for the Simulation of Turbulent Compressible Flows in Convergent-Divergent Nozzles

Daniel León-Cardona[a], Ana M. Rosso-Cerón[b,*], Julian Rodriguez-Ferreira[c], Manuel del Jesús Matínez[a], Paola A. Sanguino-Barajas[b]

[a]Mechanical Engineering Department, Universidad Industrial de Santander, Cra 27 Cll 9; Bucaramanga-Colombia
[b]Environmental Engineering Department, Unidades Tecnológicas de Santander, Calle de los Estudiantes # 9 - 82; Bucaramanga-Colombia
[c]Electrical, Electronic and Telecommunications Engineering Department, Universidad Industrial de Santander, Cra 27 Cll 9; Bucaramanga-Colombia
arosso@correo.uts.edu.co

The main objective is to analyse gas flow dynamics in a Convergent-Divergent (CD) nozzle and predict its behaviour under various conditions. The model assumes adiabatic, impermeable walls with bidimensional, compressible, steady, subsonic, and turbulent flow. Conservation equations for mass, energy, and momentum form the basis of the mathematical model, which is solved using Reynolds-Averaged Navier-Stokes turbulent models including Standard k-ε, Realizable k-ε, Standard k-ω, and Shear-Stress Transport k-ω. Evaluation of these models across different Nozzle Pressure Ratios (NPR) shows that Shear-Stress Transport k-ω correlates best with experimental data on static pressure. Three ANSYS products: DesignModeler, Meshing, and Fluent, are used for numerical simulation. The methodology reliably predicts phenomena such as flow separation, Mach disc formation, and nozzle exit regime, crucial for safe and efficient system operation.

1. Introduction

By 2026, a century will have passed since Robert Goddard introduced the CD nozzle in a liquid-fuelled rocket, a milestone replicated in almost all rocket motors to date (NASA, 2023). Technological advancements in manufacturing processes, materials, and numerical analysis methods have influenced the evolution of CD nozzles, incorporating these advances into their geometry. This has led to the emergence of alternatives to Gustav de Laval's 1888 nozzle design (Krehl, 2009).

This study analyses the impact of atmospheric pressure on the performance of rocket engines using conventional contoured or bell-shaped CD nozzles, crucial components in the contemporary space race (Mishra, 2017). As the rocket ascends vertically, the supersonic fluid expelled at the nozzle outlet undergoes an expansive regime (El-Sayed, 2016), determined by the relationship between the nozzle exit pressure and atmospheric pressure during ascent (Sutton and Biblarz, 2016). The expansion dynamics significantly influence key performance variables such as thrust and impulse. If $P_{ex} \ll P_{atm}$, overly expanded exhaust gases result in instability and thrust loss, leading to mechanical issues (Baars et al., 2012). Conversely, if $P_{ex} \gg P_{atm}$, the nozzle is under-expanded, leading to thrust loss by wasting outlet pressure. Optimal performance, generating maximum thrust, occurs when $P_{ex}=P_{atm}$ (Bahamon and Martinez, 2023). Variations from atmospheric pressure result in efficiency losses relative to optimal expansion, and since nozzle geometry is fixed (Ande and Yerraboina, 2018) while atmospheric pressure changes with altitude, the rocket motor spends limited time within the optimal performance range during ascent.

Pressure variations at the nozzle outlet, along its length and width, and their correlations with atmospheric pressure, as well as interactions with temperature, density, gas velocity, and fluid dynamic phenomena from compressible fluid interacting with the geometry, have been thoroughly studied at analytical, numerical, and experimental levels. An illustrative example is Hunter's (2004) investigation into flow separation in a flat CD nozzle across various Nozzle Pressure Ratios (NPR), incorporating experimental, theoretical, and

Paper Received: 17 January 2024; Revised: 2 June 2024; Accepted: 28 July 2024
Please cite this article as: León-Cardona D., Rosso-Cerón A.M., Rodriguez-Ferreira J., Del Jesús Matínez M., Sanguino-Barajas P.A., 2024, Assessment of RANS Turbulence Models for the Simulation of Turbulent Compressible Flows in Convergent-divergent Nozzles, Chemical Engineering Transactions, 111, 505-510 DOI:10.3303/CET24111085

computational analyses. Detailed reports include experimental static pressure measurements on the nozzle wall and results from a two-dimensional numerical simulation using the PAB3D computational fluid dynamics code. This simulation incorporates two-equation turbulence closure and Reynolds Stress Algebraic models such as Shih-Zhu-Lumley (1995), Gatski-Speziale (1993), and Girimaji (1996). Fluid density variations for these NPR are depicted through both experimental and computational Schlieren images. Conclusively, controlled separation, as demonstrated in this work, ensures the entire over-expanded nozzle performance range stays within 10% of maximum thrust efficiency. Moreover, it is established that, across the analysed NPR range, the simulated turbulence models effectively approximate experimental values, with the Shih-Zhu-Lumley model showing notable reliability.

Hunter's experimental data has become a foundational resource for validation in similar studies, where numerical simulations have been conducted for identical geometries, employing diverse turbulence models. For instance, Balabel et al. (2011) analysed the performance using specific NPR with turbulence models such as Standard k-ε (Launder and Spalding, 1972), Extended k-ε (Chen and Kim, 1987), k-ε-v^2-f (v^2-f-1) (Lien and Kalitzinm, 2001), Realizable k-ε-v^2-f (v^2-f-2) (Durbin, 1995), SST k-ω (Menter, 1994), and Reynolds Stress (Launder et al., 1975). Results indicate that SST k-ω (high-Reynolds) and realizable v^2-f models outperform others in predicting shock wave positions and separation points, with SST k-ω being particularly notable. However, the v^2-f model requires about a 20% increase in computation time. Similarly, Tolentino (2019) employed the same flat nozzle and experimental data to assess five turbulence models: SST k-ω, Standard k-ω and k-ε, Transitional k-kl-ω, and Reynolds Stress. Conclusively, based on static pressure profiles and shock wave shapes, SST k-ω is identified as the optimal model, aligning most accurately with observed shapes and experimental data.

In this work, the experimental data provided by Hunter are used as a bibliographic means of validation for the four selected turbulence models to describe and analyse the physical phenomena inside the flat nozzle. Three values of NPR were selected from the available list: 2.008, 2.412, and 3.413. The obtained static pressure profiles and density contours inside the nozzle are shown and compared with the experimental data.

2. Computational Fluid Dynamic simulation

Four RANS turbulence models are employed in computational fluid mechanics to simulate turbulence behaviour in a two-dimensional, stable, compressible, turbulent, and subsonic inlet flow within a flat nozzle with impermeable and adiabatic walls. This evaluation aims to establish the most suitable model for this specific application by comparing their strengths and weaknesses against experimental data.

2.1 Turbulence models

The mathematical model is based in the conservation of mass, energy, and momentum equations. The equation system is numerically solved using Reynolds-Averaged Navier-Stokes (RANS) turbulent models such as (ANSYS, 2021a):

Standard k-ε

This is one of the simplest and widely used RANS turbulence models. It is suitable for low and medium intensity turbulent flows but may not be suitable for high intensity turbulent flows or flow separation. It is based on two transport equations for turbulent kinetic energy and turbulent kinetic energy dissipation:

$$\frac{\partial}{\partial t}(\rho k) + \frac{\partial}{\partial x_i}(\rho k u_i) = \frac{\partial}{\partial x_j}\left[\left(\mu + \frac{\mu_t}{\sigma_k}\right)\frac{\partial k}{\partial x_j}\right] + G_k + G_b - \rho\varepsilon - Y_M + S_k \quad (1)$$

$$\frac{\partial}{\partial t}(\rho \varepsilon) + \frac{\partial}{\partial x_i}(\rho \varepsilon u_i) = \frac{\partial}{\partial x_j}\left[\left(\mu + \frac{\mu_t}{\sigma_\varepsilon}\right)\frac{\partial \varepsilon}{\partial x_j}\right] + C_{1\varepsilon}\frac{\varepsilon}{k}(G_k + C_{3\varepsilon}G_b) - C_{2\varepsilon}\rho\frac{\varepsilon^2}{k} + S_\varepsilon \quad (2)$$

Realizable k-ε

This model is an improvement over the standard k-ε model, which considers the effects of turbulence production and anisotropy in the dissipation of turbulent kinetic energy. It is more accurate than the standard k-ε and is suitable for high-intensity turbulence flows and flow separation. The modelled transport equations for k and ε in this model are:

$$\frac{\partial}{\partial t}(\rho k) + \frac{\partial}{\partial x_j}(\rho k u_j) = \frac{\partial}{\partial x_j}\left[\left(\mu + \frac{\mu_t}{\sigma_k}\right)\frac{\partial k}{\partial x_j}\right] + G_k + G_b - \rho\varepsilon - Y_M + S_k \quad (3)$$

$$\frac{\partial}{\partial t}(\rho \varepsilon) + \frac{\partial}{\partial x_j}(\rho \varepsilon u_j) = \frac{\partial}{\partial x_j}\left[\left(\mu + \frac{\mu_t}{\sigma_\varepsilon}\right)\frac{\partial \varepsilon}{\partial x_j}\right] + \rho C_1 S\varepsilon - \rho C_2 \frac{\varepsilon^2}{k+\sqrt{v\varepsilon}} + C_{1\varepsilon}\frac{\varepsilon}{k}C_{3\varepsilon}G_b + S_\varepsilon \quad (4)$$

Note that equation Eq(3) is the same as Eq(1) in the standard k-ε model, except for the model constants. However, the form of the ε equation is quite different from Eq(2). One of the notable features in this model is that the production term in Eq(4) does not involve the production of k.

Standard k-ω

The turbulent kinetic energy and the turbulent specific dissipation rate are obtained from the following transport equations:

$$\frac{\partial}{\partial t}(\rho k) + \frac{\partial}{\partial x_i}(\rho k u_i) = \frac{\partial}{\partial x_j}\left[\left(\mu + \frac{\mu_t}{\sigma_k}\right)\frac{\partial k}{\partial x_j}\right] + G_k - Y_k + S_k + G_b \quad (5)$$

$$\frac{\partial}{\partial t}(\rho \omega) + \frac{\partial}{\partial x_i}(\rho \omega u_i) = \frac{\partial}{\partial x_j}\left[\left(\mu + \frac{\mu_t}{\sigma_\omega}\right)\frac{\partial \omega}{\partial x_j}\right] + G_\omega - Y_\omega + S_\omega + G_{\omega b} \quad (6)$$

This model is more suitable for high-intensity turbulent flows and flow separation than the standard k-ε model but, may not be as accurate in low and medium-intensity turbulent flows.

Shear Stress Transport k-ω

This model combines the standard k-ω model and the standard k-ε model to take advantage of the strengths of both. It is suitable for low and high turbulence flows and is more accurate than individual models. Includes all the refinements of the Baseline k-ω (Menter, 1994) model and considers the transport of turbulent shear stress in the definition of turbulent viscosity:

$$\frac{\partial}{\partial t}(\rho k) + \frac{\partial}{\partial x_i}(\rho k u_i) = \frac{\partial}{\partial x_j}\left[\left(\mu + \frac{\mu_t}{\sigma_k}\right)\frac{\partial k}{\partial x_j}\right] + G_k - Y_k + S_k + G_b \quad (7)$$

$$\frac{\partial}{\partial t}(\rho \omega) + \frac{\partial}{\partial x_i}(\rho \omega u_i) = \frac{\partial}{\partial x_j}\left[\left(\mu + \frac{\mu_t}{\sigma_\omega}\right)\frac{\partial \omega}{\partial x_j}\right] + G_\omega - Y_\omega + D_\omega + S_\omega + G_{\omega b} \quad (8)$$

2.2 Geometry

Figure 1a illustrates the Hunter flat nozzle profile, and Figure 1b displays the dimensions of the computational domain employed in this study. Both are symmetrical and two-dimensional representations reconstructed in ANSYS using the DesignModeler tool.

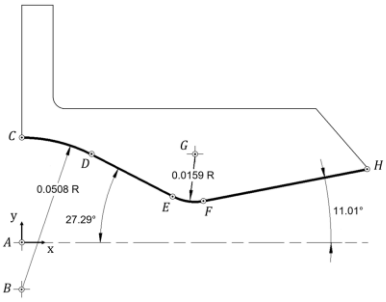

	COORDINATES [m]	
POINT	X	Y
A	0.0000	0.0000
B	0.0000	-0.0156
C	0.0000	0.0352
D	0.0233	0.0295
E	0.0505	0.0155
F	0.0608	0.0140
G	0.0578	0.0296
H	0.1156	0.0247

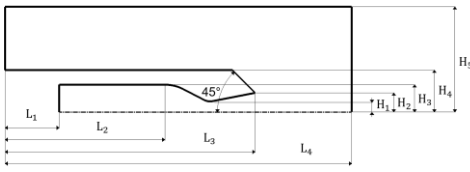

L_1	0.436 m
L_2	0.572 m
L_3	0.687 m
L_4	1.512 m
H_1	0.014 m
H_2	0.025 m
H_3	0.035 m
H_4	0.048 m
H_5	0.687 m

a. Hunter's flat nozzle

b. Dimensions of the computational domain

Figure 1: Geometry

2.3 Meshing and Computational domain

Figure 2 shows the boundary conditions, as well as the 15 bodies into which the computational domain was divided. The SST k-ω turbulence model was used within a mesh independence analysis, from which it was concluded that for this study the best structured mesh to use was the one with 3,120 elements in the subdomain (bodies 2-5) and 131,441 for the rest of the domain (bodies 1, 6-15). Mesh that presents a maximum skewness of 0.378, which is classified as "very good" within the ANSYS skewness mesh metrics spectrum (ANSYS, 2021b). A smooth transition inflation was applied to the nozzle wall, with default transition ratio (0.272), 2 maximum layers and 1.2 growth rate. For each turbulence model, 12,000 iterations were executed, which took an average of 2 hours to finish. For the analysis, ANSYS 2019 R3 was used on a Dell Precision T7500 workstation with an Intel Xeon E5620 2.4 GHz processor and 12 GB RAM.

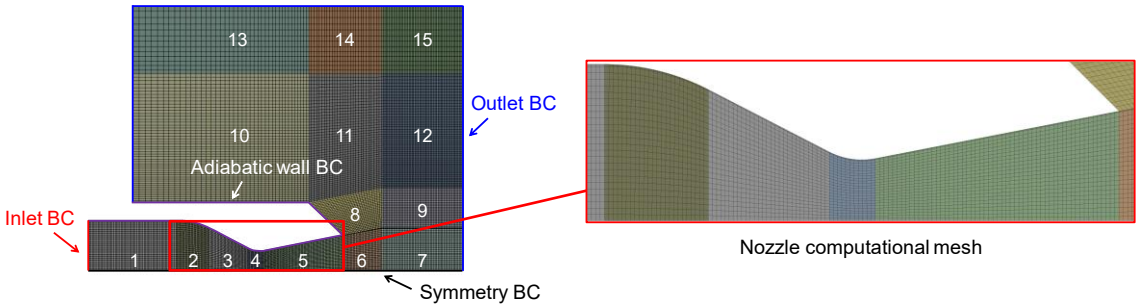

Figure 2: Part of computational domain and mesh

3. Results and analysis

Figure 3 shows the comparison of Hunter's experimental data for the selected NPR with the static nozzle wall pressure profiles obtained according to the applied turbulence model. The total sums of the relative errors of each of these experimental values with respect to their computational equivalent, the maximum relative error and the computational time of each model are also included. It's noted that the static pressure decreases as the fluid flows through the geometry of the nozzle due to the section gradually reduces, resulting in an increase in fluid velocity. Continuing from the throat area, as the flow expands, the boundary layer thickens, and the flow velocity begins to gradually decrease. This decrease will continue until the velocity is low enough for the detachment of the boundary layer to occur due to frictional forces, at which time the static pressure rise occurs.

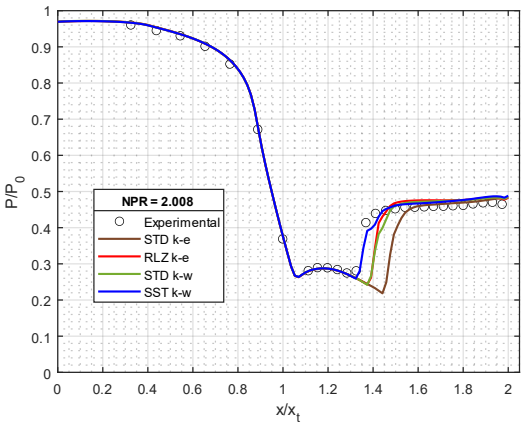

a. NPR = 2.008

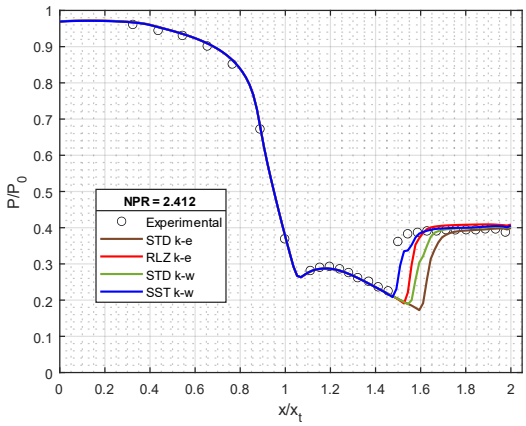

b. NPR = 2.412

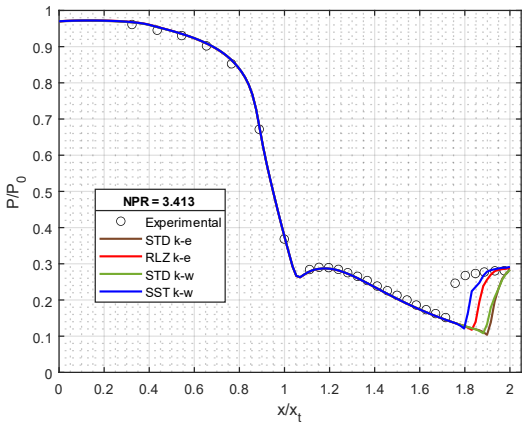

c. NPR = 3.413

	2.008	2.412	3.413	
	185.27	228.07	300.91	Error sum
STD k-ε	47.23	54.70	60.60	Maximum error
	107	110	113	Comp. time [minutes]
	122.39	147.02	213.72	Error sum
RLZ k-ε	40.80	43.98	52.65	Maximum error
	121	115	113	Comp. time [minutes]
	123.58	167.68	294.73	Error sum
STD k-ω	40.99	50.69	58.47	Maximum error
	122	135	118	Comp. time [minutes]
	69.31	83.46	167.42	Error sum
SST k-ω	9.58	29.54	49.92	Maximum error
	129	123	127	Comp. time [minutes]

d. RANS models errors

Figure 3: Comparison of experimental and computational static wall pressure profiles of the nozzle at different NPR and turbulence models

Figure 4 and Figure 5 show the Mach disks generated by the presence of a shock wave given by the supersonic expansion of the fluid in the divergent region of the flat nozzle. Its location and size depend, among other things, on the selected turbulence model and the relationship between the velocity and the static pressure of the fluid.

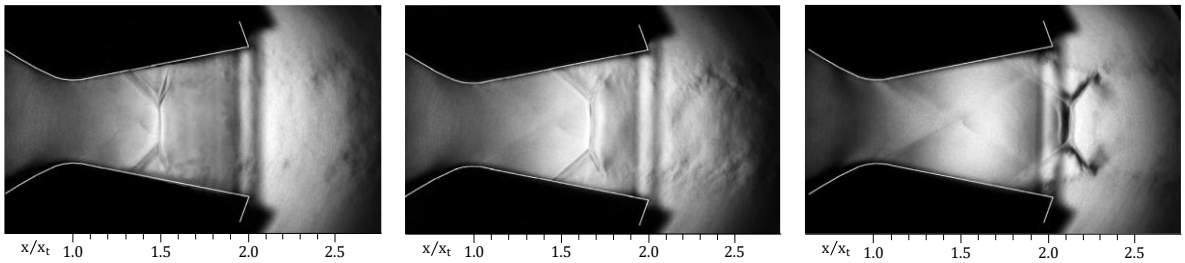

Figure 4: Experimental Schlieren flow visualization at different NPR, Hunter (2004)

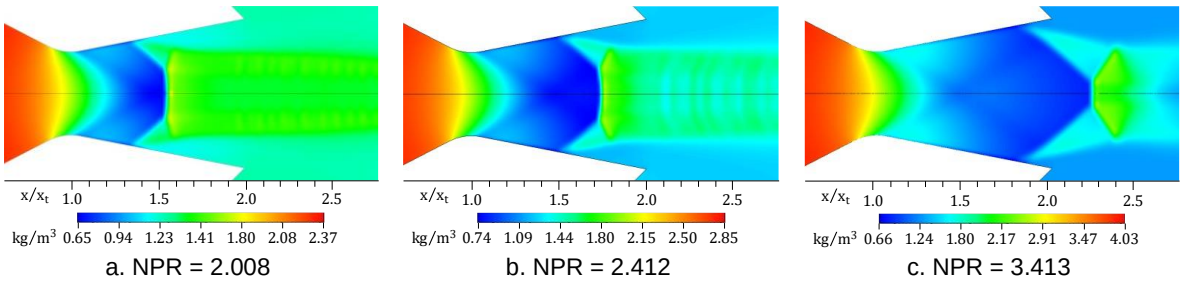

Figure 5: Density contours at different NPR for the SST k-ω model

4. Conclusions

This study has provided valuable insights into how various turbulence models perform when simulating a flat nozzle under different Nozzle Pressure Ratios (NPR). The analysis focused on specific NPR values, revealing that the turbulence models aligned well with experimental data until encountering complex turbulence related to boundary layer separation. Among the models assessed, the SST k-ω model stood out as the most effective. It demonstrated superior accuracy in representing experimental data, particularly regarding static pressure on the flat nozzle's wall and the precise location of the Mach disk in the expanding gas zone. This highlights the SST k-ω model's reliability in capturing intricate turbulence phenomena, making it suitable for future studies in similar fluid dynamics applications. Nevertheless, this greater accuracy comes at a slightly higher computational cost than the other models. The RLZ k-ε model also shows acceptable accuracy with reduced errors compared to the STD k-ε and k-ω models, making it a viable option when it's essential to balance accuracy and computational efficiency. In contrast, the STD k-ε and k-ω models have higher errors but are more computationally efficient, making them suitable for scenarios where computational resources are limited and a trade-off between accuracy and computational cost is acceptable.

The significance of the SST k-ω model in accurately characterizing the dynamic features of the flat nozzle holds substantial implications for fluid dynamics and aerospace engineering. These findings not only advance our understanding of turbulence modelling but also emphasize the critical role of selecting appropriate models for precise simulations. Future research in rocket propulsion systems and nozzle design can leverage this study's methodology and results to choose turbulence models for enhanced predictive accuracy.

Nomenclature

CD – Convergent-Divergent
C_1, $C_{1\varepsilon}$, $C_{2,}$ $C_{2\varepsilon}$, $C_{3\varepsilon}$ – constants, -
D_ω – cross-diffusion term, Pa/m^2
G_k – production of turbulence kinetic energy, Pa/s
G_b – gen. of turbulence due to buoyancy, Pa/s
G_ω – production of ω, Pa/m^2
$G_{\omega b}$ – buoyancy source for the ω equation, Pa/m^2
k – turbulent kinetic energy, m^2/s^2
NPR – Nozzle Pressure Ratios
P_{atm} – atmospheric pressure, Pa
P_{ex} – nozzle exit pressure, Pa
RANS – Reynolds-Averaged Navier-Stokes
RLZ – Realizable
S – modulus of the mean rate-of-strain tensor, s^{-1}

S_k – user-defined source terms, Pa/s
S_ε – user-defined source terms, Pa/s^2
S_ω – user-defined source terms, Pa/m^2
SST – Shear-Stress Transport
STD – Standard
u_i, u_j – fluid velocity component, m/s
Y_k – dissipation of k due to turbulence, Pa/s
Y_M – dilatation dissipation term, Pa/s
Y_ω – dissipation of ω due to turbulence, Pa/m^2
ε – turbulent kinetic energy dissipation rate, m^2/s^3
μ – molecular viscosity, kg/(m·s)
μ_t – turbulent (or eddy) viscosity, kg/(m·s)
ν – kinematic viscosity, m^2/s
ρ – density, kg/m^3
σ_k, σ_ε, σ_ω – turbulent Prandtl number, -
ω – turbulent specific dissipation rate, s^{-1}

References

Ande R., Yerraboina V.N.K., 2018, Numerical Investigation on Effect of Divergent Angle in Convergent-Divergent Rocket Engine Nozzle, Chemical Engineering Transactions, 66, 787-792.

ANSYS, Ansys Fluent Theory Guide, Release 2021 R2, ANSYS Incorporated, Canonsburg, PA, July 2021.

ANSYS, Ansys Meshing User's Guide, Release 2021 R2, ANSYS Incorporated, Canonsburg, PA, July 2021.

Baars W.J., Tinney C.E., Ruf J.H., Brown A.M., McDaniels D.M., 2012, Wall Pressure Unsteadiness and Side Loads in Overexpanded Rocket Nozzles, AIAA Journal, <doi.org/10.2514/1.J051075> accessed 25.01.2024.

Bahamon J., Martinez M., 2023, Study of fluid-dynamic behavior in a convergent–divergent nozzle by shape optimization using evolutionary strategies algorithms, Proceedings of the Institution of Mechanical Engineers, Part G: Journal of Aerospace Engineering, 237(12), 2844-2862.

Balabel A., Hegab A., Nasr M., El-Behery S., Assessment of turbulence modeling for gas flow in two-dimensional convergent–divergent rocket nozzle, Applied Mathematical Modelling, Volume 35, Issue 7, 2011, Pages 3408-3422, ISSN 0307-904X, <doi.org/10.1016/j.apm.2011.01.013> accessed 25.01.2024.

Chen Y., Kim S., Computation of Turbulent Flows using Extended k–e Turbulence Closure Model, NASA CR-179204, 1987.

Durbin P., On the k–e stagnation point anomaly, Int. J. Heat Fluid Flow 17 (1995) 89–90.

El-Sayed A., (1Ed), 2016, Fundamentals of Aircraft and Rocket Propulsion, Springer-Verlag, London, UK, 1010.

Gatski T., Speziale C., 1993, On explicit algebraic stress models for complex turbulent flows. Journal of Fluid Mechanics, 254, 59-78. doi:10.1017/S0022112093002034.

Girimaji S.S. Fully explicit and self-consistent algebraic Reynolds stress model. Theoretical and Computational Fluid Dynamics 8, 387–402 (1996) <doi.org/10.1007/BF00455991> accessed 25.01.2024.

Hunter C.A., 2004, Experimental investigation of separated nozzle flows, J. Propul. Power, 20(3), 527–532.

Krehl P., (1 Ed), 2009, History of Shock Waves, Explosions and Impact: A Chronological and Biographical Reference, Springer-Verlag, Berlin, Germany, 1288.

Launder B., Reece G., and Rodi W., Progress in the development of a Reynolds-Stress turbulence closure, Journal of Fluid Mechanics, vol. 68, no. 3, pp. 537–566, 1975. <doi.org/10.1017/S0022112075001814> accessed 25.01.2024.

Launder B., Spalding D., Mathematical Models of Turbulence, Academic, London, 1972, pp. 169–189.

Lien F., Kalitzinm G., Computations of transonic flow with the v2–f turbulence model, Int. J. Heat Fluid Flow 22 (2001) 5361.

Menter F., Two-equation eddy-viscosity turbulence models for engineering applications, AIAA J. 32 (1994) 1598–1605.

Mishra D., 2017, Fundamentals of Rocket Propulsion. Firts edition. Boca Raton: CRC Press, 482.

NASA, Dr. Robert H. Goddard, American Rocketry Pioneer, <nasa.gov/centers/goddard/about/history/dr_goddard.html> accessed 22.01.2024.

Sutton G., Biblarz O., 2016, Rocket Propulsion Elements. Ninth Edition, USA: John Wiley & Sons Ltd, 784.

Shih T., Zhu J., Lumley J.L., A new Reynolds stress algebraic equation model, Computer Methods in Applied Mechanics and Engineering, Volume 125, Issues 1-4, 1995, Pages 287-302, ISSN 0045-7825 <doi.org/10.1016/0045-7825(95)00796-4> accessed 25.01.2024.

Tolentino S. L., 2019, Evaluation of turbulence models for the air flow in a planar nozzle, Ingenius, No. 22, july-december, 25-37 <doi.org/10.17163/ings.n22.2019.03> accessed 25.01.2024.